

This article has been published in “Nanotechnology”. The final publication is available at IOP Science via <https://doi.org/10.1088/1361-6528/ab79ac>

# Ti-5Al-5Mo-5V-3Cr Bone Implants with Dual-Scale Topography: A Promising Alternative to Ti-6Al-4V

Chiara Micheletti<sup>1,2</sup>, Bryan E.J. Lee<sup>3†</sup>, Joseph Deering<sup>1†</sup>, Dakota M. Binkley<sup>1</sup>, Simon Coulson<sup>1,4</sup>, Asad Hussain<sup>1</sup>, Hatem Zurob<sup>1</sup>, Kathryn Grandfield<sup>1,3\*</sup>

1 Department of Materials Science and Engineering, McMaster University, Hamilton, ON, Canada

2 Department of Chemistry, Materials and Chemical Engineering, Politecnico di Milano, Milan, Italy

3 School of Biomedical Engineering, McMaster University, Hamilton, ON, Canada

4 Additive Manufacturing Innovation Centre, Mohawk College, Hamilton, ON, Canada

† Authors contributed equally

\* Corresponding author:

Prof. Kathryn Grandfield

McMaster University

1280 Main Street West

Hamilton, ON, L8S 4L7

Canada

Email: [kgrandfield@mcmaster.ca](mailto:kgrandfield@mcmaster.ca)

## ABSTRACT

Modifications to the compositional, topographical and morphological aspects of bone implants can lead to improved osseointegration, thus increasing the success of bone implant procedures. This study investigates the creation of dual-scale topography on Ti-5Al-5Mo-5V-3Cr (Ti5553), an alloy not presently used in the biomedical field, and compares it to Ti-6Al-4V (Ti64), the most used Ti alloy for bone implants. Dual-scale surface topography was obtained by combining selective laser melting (SLM) and electrochemical anodization, which resulted in micro- and nanoscale surface features, respectively. Ti5553 and Ti64 samples were manufactured by SLM and showed comparable surface topography. Subsequent electrochemical anodization succeeded in forming titania nanotubes (TNTs) on both alloys, with larger nanotubes obtained with Ti5553 at all investigated anodization voltages. At an anodization voltage of 40 V, a minimum time of 20 min was necessary to have nanotube formation on the surface of either alloy, while only nanopores were evident for shorter times. Seeded Saos-2 cells showed ideal interactions with surface-modified structures, with filopodia extending to both surface microparticles characteristic of SLM and to the interior of TNTs. Attractiveness of Ti5553 lies in its lower elastic modulus ( $E = 72$  GPa) compared to Ti64, which should mitigate stress-shielding phenomena *in vivo*. This, combined with the analogous results obtained in terms of dual-scale surface topography and cell-substrate interaction, could indicate Ti5553 as a promising alternative to the widely-employed Ti64 for bone implant device manufacturing.

**Keywords:** bone implant, TiO<sub>2</sub> nanotubes, SLM, anodization, Ti-5Al-5Mo-5V-3Cr, Ti-6Al-4V, surface topography

# 1 INTRODUCTION

Titanium and its alloys are commonly utilized in the biomedical field for bone implant fabrication due to the presence of an amorphous titania surface layer that spontaneously forms during oxidation [1] and results in excellent corrosion resistance and biocompatibility.

Additive manufacturing techniques such as selective laser melting (SLM) and electron beam melting (EBM) have recently emerged as methods to fabricate Ti-based bone implants, as they enable users to produce highly customized parts and unique devices to meet patients-specific needs. SLM and EBM are powder bed fusion techniques where the component is manufactured layer-by-layer by progressively melting and sintering metal powders with a laser or electron beam [2,3]. Moreover, SLM generates components with microrough surfaces, without the need for post-processing operations. This inherent microscale surface topography is characterized by the presence of a random distribution of loosely sintered spherical particles due to insufficient energy density for sintering [4] and balling effects during processing [5]. These microscale features can be beneficial for the bonding between bone and titanium implant, termed osseointegration [6,7], where implant surface is known to play a major role for *in vitro* cell behaviour [8] and *in vivo* osseointegration [9].

Since poor osseointegration is detrimental for the success of an implant procedure, surface modification strategies to improve this aspect are extensively studied. Not only microscale, but also nanoscale topography is believed to improve osseointegration [10,11]. While the relationship between microscopic surface features and osseointegration has been well characterized in the literature [6,12,13], precise understanding of nanoscale interactions during osteogenesis is limited [14]. Nanopatterning has been shown to be beneficial for cell adhesion due to the increase in protein adsorption from the extracellular matrix [14]. The combination of microscale topography with nanoscale surface features can improve primary fixation with a dual-scale approach that improves cellular adhesion, migration, proliferation, and differentiation on the implant surface [15].

Dual-scale topography can be obtained by using electrochemical anodization to create titania nanotubes (TNTs) on the microrough surface of additively manufactured implant materials [16]. Electrochemical anodization is a well-characterized method to generate self-ordered arrays of TNTs as a result of competition between oxidation and dissolution reactions occurring on titanium in presence of fluoride-based electrolytes [17]. A dual-scale surface modification strategy aimed to combine micro- and nanoscopic features has been investigated for Ti-6Al-4V (Ti64) [18], which is currently the most widely used titanium alloy for bone implants. Despite its extensive use as a bone implant material, a significant drawback of Ti64 is its significantly greater elastic modulus compared to trabecular and cortical bone [19,20], due to the  $\alpha$ -Ti phase fraction [21]. This mismatch of elastic modulus can cause stress-shielding, a condition where the density of bone tissue near the implant material is reduced due to a lack of biomechanical force [22], and bone atrophy in post-operative conditions [23]. An increase in  $\beta$ -phase fraction in titanium microstructures can result in a lower elastic modulus, thereby reducing the likelihood of aforementioned post-operative conditions. Therefore, alloy compositions with higher levels of  $\beta$ -

stabilizing elements are being developed to optimize the mechanical properties of bone implants [24]. Herein, we investigate one such alloy by studying a near- $\beta$  titanium alloy, i.e. Ti-5Al-5Mo-5V-3Cr (Ti5553). Ti5553 was chosen not only for its lower elastic modulus, but also for its processability by SLM already confirmed by previous studies [25–27]. However, such studies all focused on the application of Ti5553 in the aerospace industry, given the present use of this alloy for structural components in airplanes [28]. Therefore, this alloy has both demonstrated ease of printing, and potentially favorable mechanical properties for biological applications. Tensile mechanical properties of Ti5553 including elastic modulus, yield strength, ultimate tensile strength and ductility were measured. This work aims to evaluate the creation of dual-scale topography combining SLM and anodization on Ti5553, which, to our knowledge, has not been previously investigated. Electrochemical anodization was carried out with different parameters to investigate the role of time and voltage on the final surface morphology. An *in vitro* study of the biological response was completed by imaging osteosarcoma cells cultured on the sample surface with scanning electron microscopy (SEM). Bioactivity of the anodized surfaces was also qualitatively assessed in simulated body fluid (SBF). To compare this novel biomedical alloy with the current gold standard, i.e. Ti64, dual-scale topography was obtained on the latter using the same procedure as for Ti5553. Ti64 samples were then similarly characterized in terms of surface and biological properties.

## 2 MATERIALS AND METHODS

### 2.1 Fabrication of Specimens by Additive Manufacturing

Ti5553 and Ti64 samples were additively manufactured by a SLM machine (EOSINT M280, EOS GmbH, Munich, Germany). Plasma-atomized Ti5553 and Ti64 powders (purchased from AP&C, GE Additive, Boisbriand, Canada) with a respective size range of 25-63  $\mu\text{m}$ , and 15-45  $\mu\text{m}$  were utilized. Samples with a 10 mm x 10 mm x 1 mm square base, and a 3 mm x 10 mm x 1 mm handle (Figure 1) were printed according to the parameters presented in Table 1 using a single bulk exposure and two subsequent contour exposures. After manufacturing, the 3D-printed parts were cleaned by ultrasonication in ethanol, acetone and deionized water for 15 min, 15 min and 5 min, respectively. Ethanol, acetone and deionized water were employed as commonly used solvents to clean the surface without altering it.

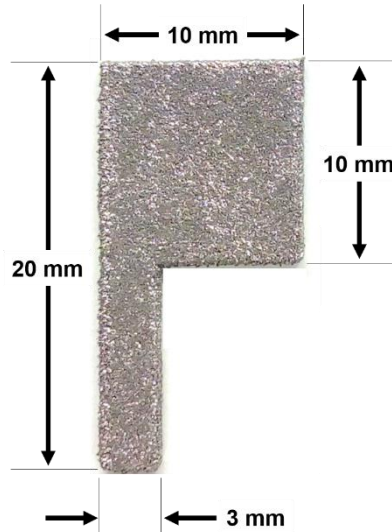


Figure 1: Geometry and dimensions of samples manufactured by SLM.

Table 1: Processing parameters used for the fabrication of Ti5553 and Ti64 by SLM.

Parameter	Bulk	Contour
Laser Power (W)	340	190
Scanning Speed (mm/s)	1250	1250
Hatch Spacing (mm)	0.120	0.060
Layer Thickness (mm)	0.060	0.060
Energy Density ( $J/mm^3$ )	37.8	42.2

## 2.2 Mechanical Characterization

Sub-size tensile bars were machined from SLM Ti5553 according to specifications set by ASTM E8 with the axial direction equivalent to the x-direction on the build plate. Samples were loaded up to 12.0 kN of applied load, relaxed to 2.4 kN, reloaded to 14.0 kN, relaxed to 2.8 kN, and then loaded to fracture under a constant strain rate of 1.5 mm/min. All measurements were recorded in triplicate. The average elastic modulus was calculated from the unloading portions of the resulting stress-strain plots to avoid potential grip movement effects during loading. The 0.2% offset yield strength, ultimate tensile strength, and ductility were also identified for each sample.

## 2.3 Electrochemical Anodization

By mounting the 3D-printed sample at the handle, the square portion was immersed into a solution of ethylene glycol (certified grade, Sigma Aldrich) with 0.3 wt.% ammonium fluoride (certified

grade, Fisher Chemical) and 2 vol.% deionized water. A (25 x 25 x 0.13) mm platinum foil (Sigma Aldrich) was used as counter-electrode. The 3D-printed sample and the Pt electrode were connected to an EPS 2A200 power supply (Hoefer Inc., Holliston, USA) as anode and cathode, respectively. The electrolyte was magnetically stirred for 15-20 min prior usage to ensure solution homogeneity, and it was kept gently stirred during the entire anodization process. Fresh solution was employed for each sample. Four different anodization voltages: 20 V, 40 V, 60 V and 80 V, were tested at a fixed time of 30 min. Additional samples were anodized at a constant voltage of 40 V for 5 min, 10 min, 20 min and 60 min. After anodization, the handle was detached from the square portion of the sample and discarded. All the anodized samples were ultrasonicated in ethanol for 30 s.

## *2.4 Surface Characterization*

Microscale roughness of the samples manufactured by SLM was characterized with an Alicona Infinite Focus G5 optical profilometer (Alicona Imaging GmbH, Graz, Austria) on three characteristic 3 mm x 3 mm areas of each sample. In each area, linear roughness parameters ( $R_a$ ,  $R_q$ ,  $R_z$ ) were measured along three different directions: two orthogonal to each other and one at 45°. Values obtained were then statistically averaged. Surface area roughness parameters, i.e.  $S_a$ ,  $S_q$  and  $S_z$ , were also evaluated.

The surfaces of samples prior to (microscale topography) and after anodization (dual-scale topography) were imaged by SEM. Secondary electron images were acquired with acceleration voltages of 2-3 kV using a JSM-7000F SEM (JEOL, Peabody, USA) or a Magellan 400 SEM (ThermoFisher Scientific, Hillsboro, USA). For both as-printed Ti5553 and Ti64, the average size of the microspherical particles present on the surface was computed by measuring the diameter of 30 particles in a representative 350  $\mu\text{m}$  x 350  $\mu\text{m}$  area of a SEM micrograph using ImageJ (NIH, Bethesda, USA) and averaging the results. On the samples anodized at 20 V, 40 V, 60 V and 80 V for 30 min, TNT diameter was measured using ImageJ (NIH, Bethesda, USA) by applying a grayscale threshold to micrographs and treating nanotubes as ellipsoids, so their maximum and minimum axes were averaged to obtain the nanotube diameter. After determining the diameter of all the nanotubes in a SEM micrograph, measurements were averaged to obtain the final TNT diameter representative of a certain anodization condition. Regions with collapsed or irregular nanotubes were omitted from the analysis.

Surface wettability prior to and after anodization was determined by evaluating the water contact angle (OCA35, Dataphysics Instruments GmbH, Filderstadt, Germany), whereby a smaller angle is indicative of increased wettability. Measurements were completed in triplicate.

## *2.5 Biological Characterization*

Saos-2 cells (ATCC®) were cultured on Ti5553 and Ti64 specimens, both as-printed (microscale topography) and after anodization at 40 V for 30 min (dual-scale topography), according to methods developed by Lee et al. [29]. After a 1-day culture period, cells were fixed with 0.25% glutaraldehyde in sodium cacodylate before staining with osmium tetroxide. Afterwards, dehydration was conducted in graded concentrations of ethanol from 25% to 100% (in milli-Q

water). Finally, samples were critical point dried and coated with 10 nm of Pt prior to imaging with SEM. A Tescan VP SEM (Tescan, Brno, Czech Republic) operated at 10 kV was used to image cells cultured on the as-printed samples, while a JSM-7000F SEM (JEOL, Peabody, USA) was used to analyze the anodized samples.

Ti5553 and Ti64 samples in the as-printed condition and anodized at 40 V for 30 min were immersed in 25 mL of SBF (Hanks' balanced salts solution without sodium bicarbonate, Sigma-Aldrich) and stored at 37 °C for 3-day and 7-day periods to assess the bioactivity of the surfaces. SEM and energy dispersive X-ray spectroscopy (EDX) (Aztec, Oxford Instruments, USA) were used to characterize crystalline deposits on the sample surface after rinsing in deionized water and drying in air.

## 2.6 Statistical Methods

Statistical software R (R Core Team, Auckland, New Zealand) was used for statistical analysis. Values of roughness, size of microparticles on the surface and contact angle of as-printed Ti5553 and Ti64 were compared by Welch's independent two-tailed independent t-test to assess whether differences between the two alloys were statistically significant. Two-way ANOVA and Tukey's HSD test were also used to compare the wettability and the TNT diameter at each voltage for Ti5553 and Ti64 after anodization. Significance level was set at  $\alpha = 0.05$ .

# 3 RESULTS

## 3.1 Fabrication of Specimens by Additive Manufacturing

SEM imaging of the 3D-printed samples showed the presence of particles randomly distributed on the surface as a result of SLM. Particle dimensions within a representative 350  $\mu\text{m}$  x 350  $\mu\text{m}$  area of a SEM micrograph were measured (Figure 2). As expected, Ti5553 had a higher fraction of particles smaller than 20  $\mu\text{m}$  and Ti64 had a higher fraction of particles larger than 35  $\mu\text{m}$ , due to the initial size distribution of bulk powder. In the intermediate range of 20-35  $\mu\text{m}$ , no distinct difference in surface particle size was noted. The average particle diameter in the sampled surface was 27  $\mu\text{m}$  for Ti5553 and 26  $\mu\text{m}$  for Ti64, but the difference was found to be not statistically significant.

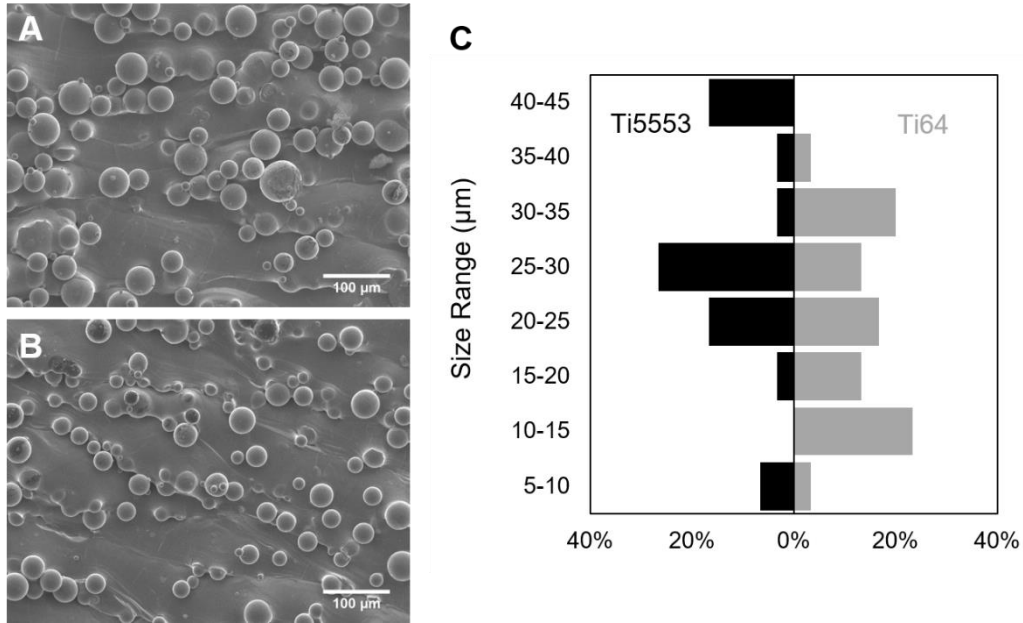


Figure 2: Representative view of microscopic particles on the as-printed surface of (A) Ti5553 and (B) Ti64. (C) Size distribution of surface particles in 350 μm x 350 μm examination area for alloys.

### 3.2 Mechanical Characterization

Stress-strain curves determined by uniaxial tensile test of Ti5553 samples are reported in Figure 3. Relevant mechanical property data, i.e. elastic modulus (E), yield strength (YS), ultimate tensile strength (UTS), and ductility are summarized in Table 2. The repeated loading procedure was successful in obtaining two measurements of the elastic modulus for each specimen. The elastic modulus for Ti5553 (72 GPa ±3 GPa) showed little deviation between unloading portions of the stress-strain curves for all three samples. No anomalies were noted between strain at fracture, yield strength, or tensile strength in any of the three samples, indicating that processing parameters produced a uniform structure in the x-direction of the build path. All specimens displayed ductile fracture surfaces and fractured within the reduced section.

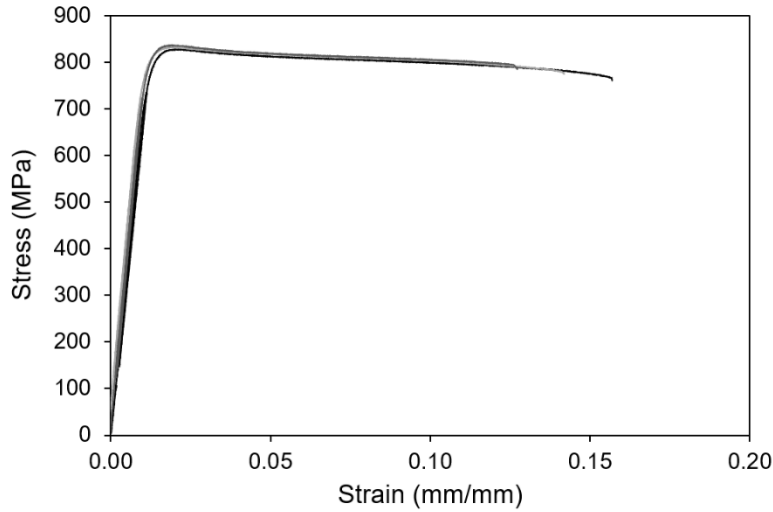


Figure 3: Stress-strain curves resulting from uniaxial tensile tests of three different specimens of Ti5553.

Table 2: Mechanical properties of Ti5553 in uniaxial tension.

E [GPa]	YS [MPa]	UTS [MPa]	Ductility [%]
$72 \pm 3$	$807 \pm 7$	$832 \pm 4$	$14 \pm 2$

### 3.3 Electrochemical Anodization

3D-printed samples anodized for 30 min showed evidence of titania nanotube development on both the microspherical particles and the underlying substrate at all tested voltages, as assessed by SEM imaging (Figure 4). The presence of cracks between nanotube clusters both on the microspheres and uneven portions of the substrate were also observed (Figure 5).

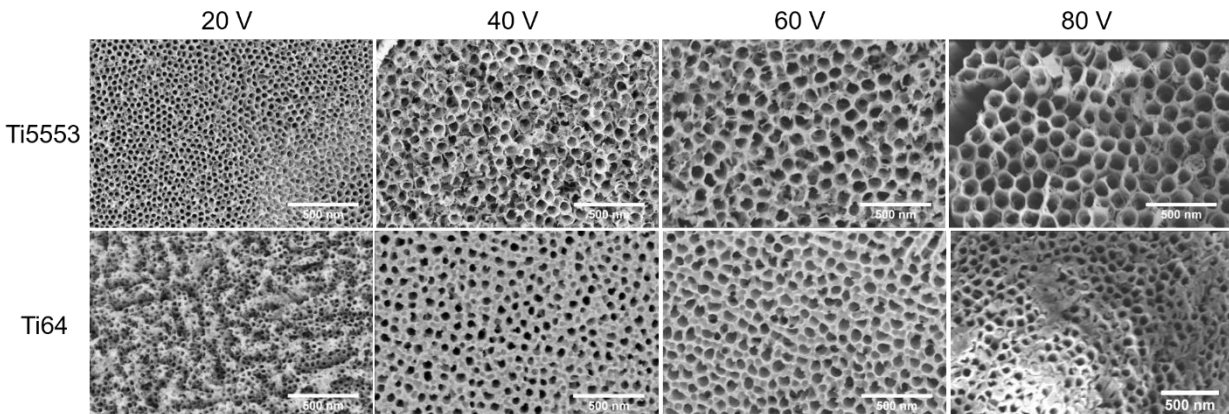


Figure 4: Titania nanotubes obtained after 30-min anodization of Ti5553 and Ti64 at 20 V, 40 V, 60 V and 80 V.

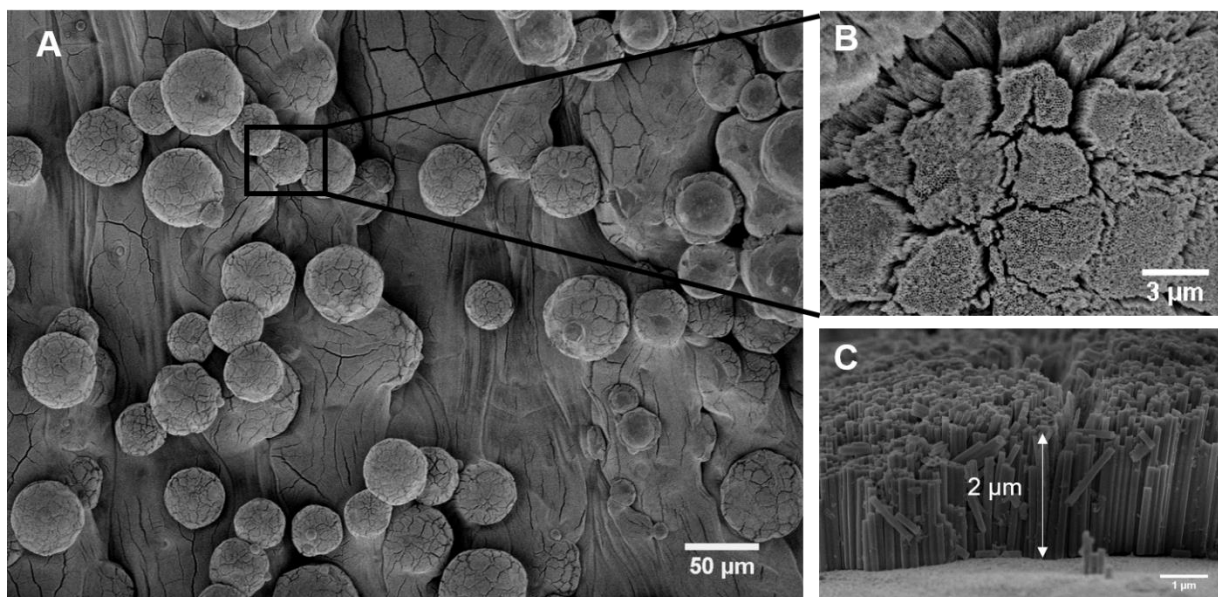


Figure 5: Surface of Ti5553 anodized at 80 V for 30 min showing considerable crack formation. (A,B) Cracks separate the TNTs in distinct arrays, especially on the spherical particles. (C) Cracking enabled approximate estimation of nanotube length, on this specimen around 2  $\mu\text{m}$ .

For both alloys, an increase in the anodization voltage led to the formation of larger nanotubes (Figure 6). Ti64 anodized at 80 V differed from this trend, as the nanotube diameter was smaller than that of samples anodized at 60 V. For all the anodization voltages investigated, Ti5553 nanotubes were larger than those of Ti64 ( $p < 0.001$ ). Some irregular nanotubes morphologies and structures, such as nanograss and double-walled nanotubes (Figure 7), were observed on some anodized samples of both alloys, and more frequently for Ti5553 than Ti64. Ti5553 and Ti64 showed a similar evolution of the TNT morphology as a function of anodization time, when keeping the voltage at 40 V. Characteristic nanotube morphologies were associated with each time interval, as shown in Figure 8. After 5 min and 10 min, a nanoporous, precursor structure to nanotube formation was observed. The quantity of nanopores increased at the 10 min-interval compared to the 5 min-interval. Distinct arrays of nanotubes were visible on both the substrate and microspheres after 20 min, with a similar morphology to samples anodized for 30 min. Some areas with extended nanograss formation were more evident after 60 min.

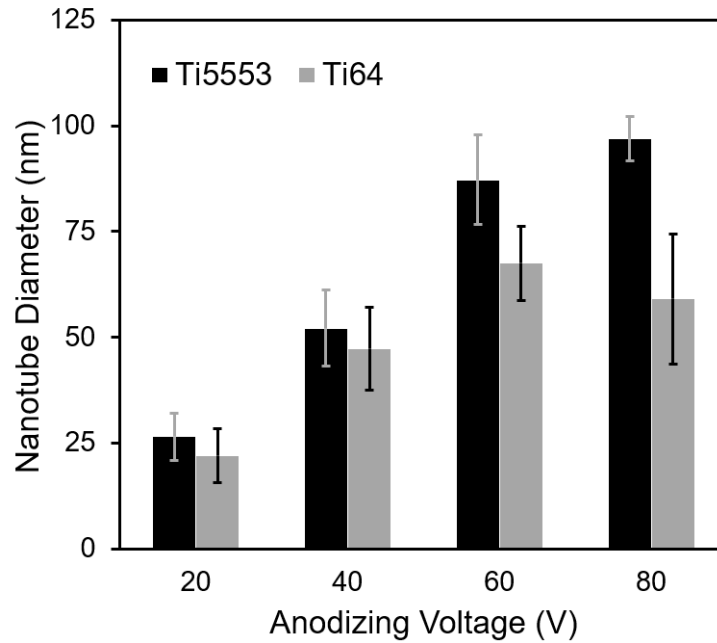


Figure 6: Average nanotube diameter for Ti5553 and Ti64 after anodization for 30 min at each voltage indicated in the graph. Statistical significance ( $p < 0.05$ ) was confirmed for all the groups.

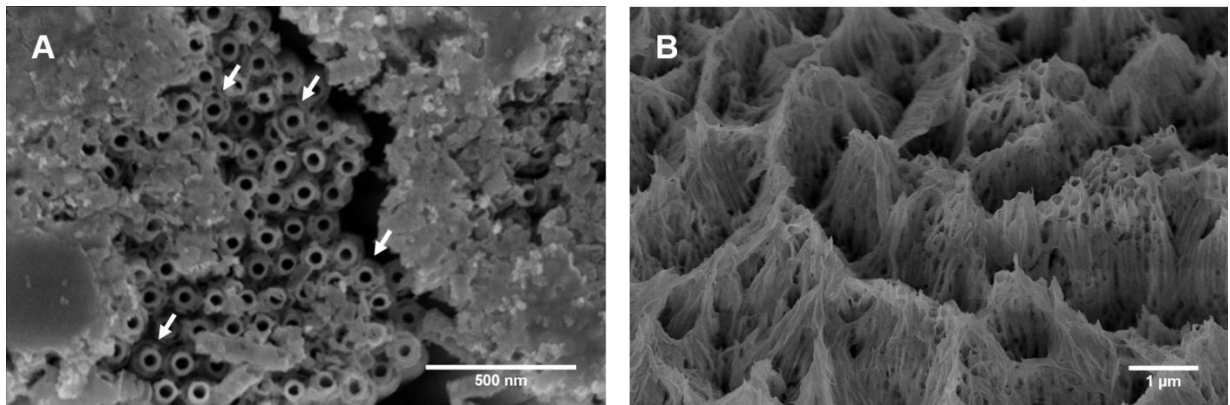


Figure 7: Irregular nanotube morphologies including: (A) Double-walled nanotubes on Ti5553 anodized at 60 V for 30 min. (B) Nanograss formation on Ti64 after anodization at 80V for 30min.

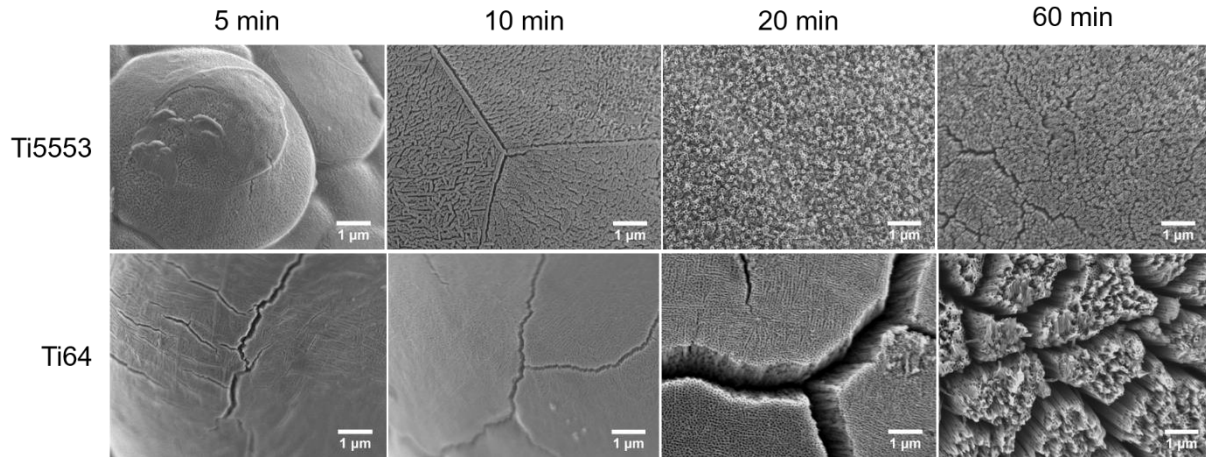


Figure 8: Nanotube morphology on the surface of both alloys at constant 40 V for varying times. Regular nanotube formation occurs by 20min, with crack and nanogras frequency increasing over time.

### 3.4 Surface Characterization

Relative measurements for Ti5553 and Ti64 (Figure 9) extracted from a surface profilometer showed significance ( $p < 0.05$ ) in peak surface roughness by two-sample t-test. Ti5553 had higher average roughness measurements across the entirety of the surface, which corresponds to the larger particle size distribution of the powder.

Alloy	$R_a$ [ $\mu\text{m}$ ]	$R_q$ [ $\mu\text{m}$ ]	$R_z$ [ $\mu\text{m}$ ]	$S_a$ [ $\mu\text{m}$ ]	$S_q$ [ $\mu\text{m}$ ]	$S_z$ [ $\mu\text{m}$ ]
Ti5553	$15.6 \pm 1.7^*$	$19.1 \pm 2.2^*$	$56.6 \pm 4.6^*$	$16.9 \pm 0.3$	$21.0 \pm 0.1$	$152.9 \pm 4.5^*$
Ti64	$13.0 \pm 3.0^*$	$15.6 \pm 3.6^*$	$48.4 \pm 10.1^*$	$14.3 \pm 1.2$	$17.5 \pm 1.4$	$125.1 \pm 9.9^*$

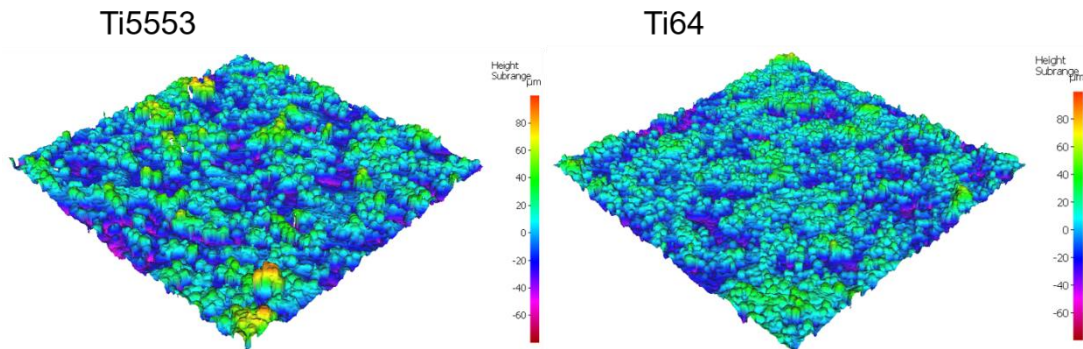


Figure 9: Area roughness measurements for as-printed Ti5553 and Ti64. \* denotes statistical significance ( $p < 0.05$ ).

Water contact angle (CA) for the as-printed Ti5553 ( $CA = 79.1^\circ \pm 3.6^\circ$ ) and Ti64 ( $CA = 78.2^\circ \pm 7.2^\circ$ ) showed slight hydrophilic behaviour for both alloys. The contact angle for both alloys significantly decreased after anodization to values ranging between  $(9.6 \pm 1.1)^\circ$  and  $(13.3 \pm 4.9)^\circ$ ,

demonstrating increased surface wettability. No noticeable difference was observed in the two alloys and among the anodization voltages tested ( $p < 0.05$ ).

### 3.5 Biological Characterization

SEM micrographs showed the presence of Saos-2 cells after 1-day of growth on the surface of both alloys, before and after anodization. This could be indicative of the non-cytotoxicity of the materials. The cells displayed an extended and stretched morphology on both the flatter areas and microspheres of the 3D-printed samples (Figure 10). In case of the anodized samples, the filopodia of the cells seemed to extend to both the surface and into the depth of the nanotubes.

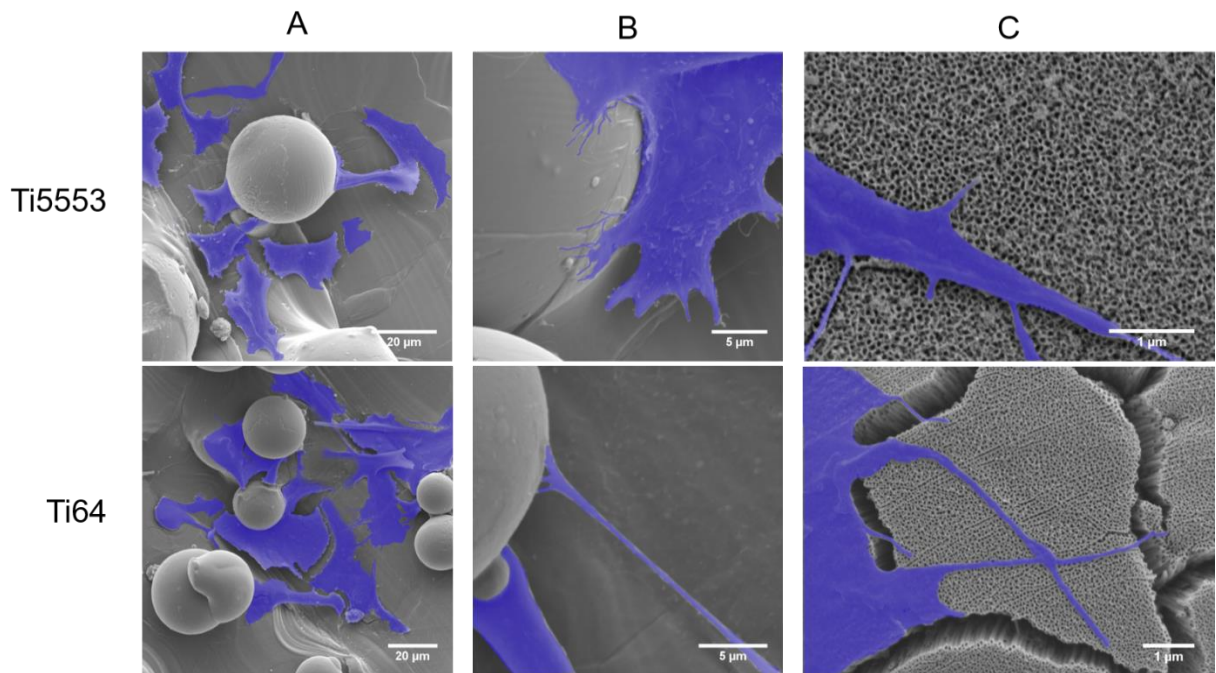


Figure 10: Saos-2 cells (coloured in blue) adhering on Ti5553 and Ti64 surface after a 1-day culture period. (A,B) Cells and filopodia extension to reach microspherical surface particles on as-printed samples. (C) Interaction between cells and nanotubes on anodized samples.

Both as-printed and anodized samples showed limited presence of calcium phosphate precipitates after a 3-day immersion in SBF solution. After 7 days, more precipitates were present on the surface, as revealed by SEM. Moreover, Ca and P on the 7-day EDX spectra (Figure 11) suggested that these precipitates could be indicative of the nucleation of calcium phosphates, such as hydroxyapatite or others. The other signals present in Figure 11 are associated with the elements composing the alloy. No observable difference in quantity of precipitate formation was noticed between Ti5553 and Ti64, thus suggesting a comparable *in vitro* bioactivity of the two alloys.

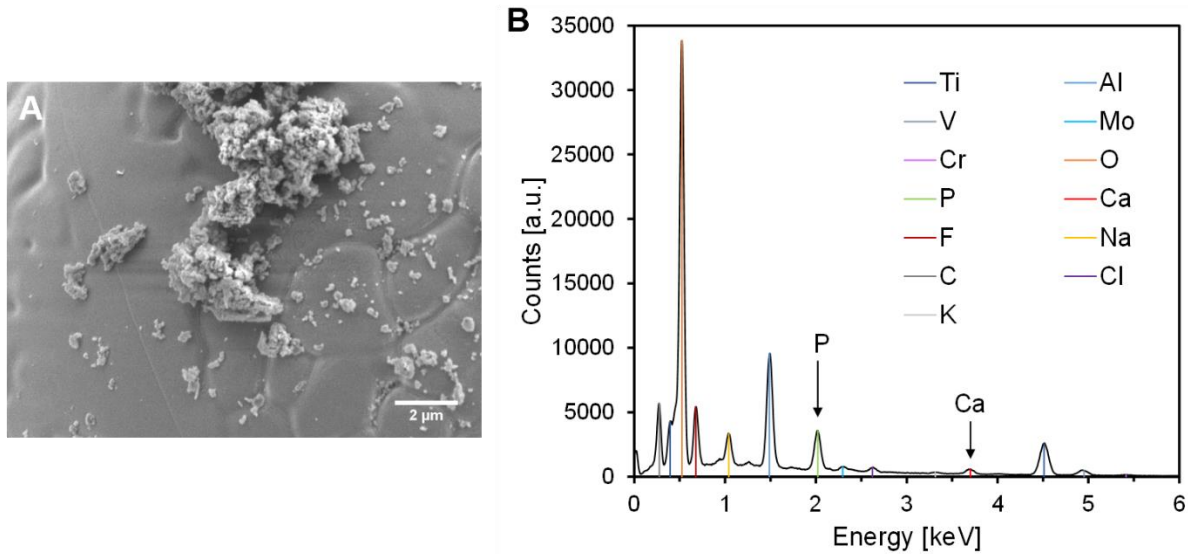


Figure 11: (A) SEM micrograph showing precipitates on the surface of as-printed Ti5553 after 7 days of immersion in SBF. (B) Corresponding EDX spectrum. Ca and P peaks could be indicative of the nucleation of calcium phosphates.

## 4 DISCUSSION

### 4.1 Dual-Scale Topography and TNTs Morphology

With the aim of improving osseointegration of Ti alloys-based bone implants, the approach of creating samples with a dual-scale surface topography by the combination of SLM and electrochemical anodization was previously proposed for Ti64 by Gulati et al. [18]. This study proved this method to be successful on Ti5553 for the first time. Moreover, the outcomes for Ti64 were analogous to what found by Gulati et al. [18], although different anodization conditions (electrolyte, voltage, time) were used in this study. Ti5553 and Ti64 samples manufactured by SLM using the same process parameters showed comparable surfaces with a microscale topography (Figure 2). While the creation of TNTs by electrochemical anodization has been well documented on Ti64 [18,30] and other biomedical alloys [17], nanotube obtainment and characterization in the near- $\beta$  alloy Ti5553 had not yet been documented before this study. Nanotube morphology was comparable for Ti5553 and Ti64 when time was varied at fixed voltage (Figure 8). When anodizing for the same time at different voltages, nanotubes obtained on Ti5553 had a larger diameter than those on Ti64 ( $p < 0.05$ ) (Figure 6). With the exception of Ti64 anodized at 80 V, nanotube size in both materials increased linearly with the applied anodization voltage. This is in accordance with previous findings for flat unalloyed titanium [17,31], therefore suggesting that neither the presence of alloying elements nor the micro-scale topography of the substrates affected nanotube size. At higher anodization voltages, nanotubes appeared to be more likely to collapse and merge with neighbours due to a more extensive etching, resulting in the formation of a nanograss network [32]. This could explain why nanotubes obtained on Ti64 anodized at 80 V were smaller than those obtained at 60 V. The higher etching at 80 V may have promoted collapse of bigger nanotubes, hence only the smaller ones maintained their structural

integrity. However, Ti5553 showed a higher stability than Ti64 when anodized at 80 V, as the linear trend between anodization voltage and nanotube diameter was retained. The dissimilar behaviour could be attributed to the presence of different alloying elements. This is believed to also justify the presence of areas with double-walled tubes (Figure 7), which were sometimes observed for Ti5553, probably as a consequence of selective dissolution of different alloying elements during anodization [33].

Some studies on unalloyed Ti samples have correlated TNTs diameter and cellular activity, with good cellular activity usually occurring for diameters ranging from 30 to 50 nm [34]. As new titanium alloys are developed and subsequently anodized, it is important to understand the parameters necessary to control the diameter and thus optimize cell-surface interactions. This work demonstrated that the diameter of TNTs for Ti5553 and Ti64 is different under the same anodization conditions, and therefore the two alloys may lead to different cell responses both *in vitro* and *in vivo*. The better stability of bigger nanotubes identified for Ti5553 compared to Ti64 would make Ti5553 more suitable for applications requiring larger nanotubes, such as local drug delivery, when higher drug-loading capacity is desired [35].

Parts produced by SLM are often post-processed, such as by sandblasting and chemical etching, to remove the unmelted particles present on the surface that may be released *in vivo* [36]. However, in this work, 3D-printed samples were not subjected to any form of post-processing in order to exploit their inherent microrough surface topography. Therefore, further studies would be required to assess whether the microparticles on the surface could detach and be released in the organism. Nevertheless, bone implants of Ti64 manufactured by SLM and not subjected to any post-processing have already been tested *in vivo* with positive outcomes [37].

The presence of cracks separating well-defined arrays of TNTs was noticed for both Ti5553 and Ti64. Crack formation can be attributed to the outward growth mechanism of the nanotubes perpendicularly from the surface, combined with the internal stress build-up on curved surfaces [38]. The side-view of the TNTs (Figure 5) offered by the presence of cracks confirmed that deep tubular structures were forming under sufficient anodizing conditions, rather than the nanoporous structures observed for short anodization times. Cracks may compromise the stability and adhesion of the TNT film, in turn negatively affecting the success of a bone implant procedure. Some approaches to reduce crack nucleation, such as using aged instead of fresh electrolyte, have been suggested by others [38] but not explored in this work.

## 4.2 Biocompatibility and Bioactivity

After a 1-day culture period, Saos-2 cells showed good attachment on as-printed Ti5553 surfaces. Cell-surface interaction appeared to be improved by the anodization treatment and the resulting dual-scale topography. In fact, it was observed that the surface features promoted the anchoring of Saos-2 cells, as their filopodia extended from the microspheres to the inner cavity of individual nanotubes (Figure 10), confirming what has previously been reported in literature [39]. Analogous behaviour in terms of cell responses was identified for Ti64, hence suggesting similar biocompatibility of the two alloys. However, further studies would be necessary to evaluate cell viability and eventual cytotoxicity of the substrates of both alloys at longer time points.

Both Ti5553 and Ti64 anodized samples displayed a much higher surface wettability than the as-printed specimens, verifying what has been observed for anodized titanium in other works [40]. This increased hydrophilicity could be important to promote initial wetting of the implant after placement, consequently enhancing wound healing and osseointegration [41]. However, the anodized surfaces may tend to become more hydrophobic over time [42]. Hydrophilicity could be restored by exploiting the photocatalytic properties of TiO<sub>2</sub> [43].

Traces of Ca and P revealed by EDX after 7-day immersion in SBF (Figure 11) could be indicative of the formation of calcium phosphates, such as hydroxyapatite or others, thus predicting good bioactivity *in vivo* [44]. Further evaluation of this coating composition could be confirmed with longer immersion time points that might yield sufficient coating thickness for analysis with X-ray diffraction (XRD).

### 4.3 Mechanical Characterization

Ti5553 has been previously investigated for high strength and easily controlled microstructure [45], which can also be beneficial for implant applications. When designing bone implants, the elastic modulus of the material is also an important parameter to take into account, as stress-shielding has to be considered.

The presence of  $\beta$ -stabilizing elements in Ti5553 succeeded in reducing the elastic modulus by 37% relative to literature values of additively manufactured Ti64 ( $E = 113 \text{ GPa} \pm 5 \text{ GPa}$  [19]). However, a decrease in yield strength and ultimate tensile strength was observed for Ti5553 compared to what reported in literature for Ti64 (YS and UTS around 1075 MPa and 1199 MPa, respectively [19]). Heat treatment of the  $\beta$ -alloy is likely to increase the strength to values comparable to  $\alpha+\beta$  Ti alloys like Ti64 without sacrificing the low-stiffness achieved by alloying [24]. The reduced stiffness mismatch between Ti5553 and bone could aid in mitigating stress-shielding effects and reducing bone atrophy after implantation compared to many conventional biomedical alloys with a higher elastic modulus.

## 5 CONCLUSIONS

The implant surface plays a major role in successful osseointegration; thus, it is important to modify the surface to create optimal features capable of promoting cellular interactions. SLM was employed successfully to obtain Ti5553 and Ti64 samples with a microscale surface topography. Compared to the more-widely investigated Ti64 substrate, Ti5553 displayed similar anodization behaviour, with larger nanotube diameter obtained for the same process conditions. Compared to the as-printed samples, anodized specimens of both alloys showed increased interactions between cell and surface features. The possibility to create a dual-scale surface topography using SLM and anodization with similar outcomes as Ti64, combined with the lower elastic modulus, suggests a potential use of Ti5553 as a bone implant material. Future work should focus on the *in vitro* and *in vivo* response of surface-modified Ti5553, as well as selective parametric analysis for SLM conditions to optimize surface topography. Moreover, the stability and adhesion of the nanotube

layer on the 3D-printed substrates should also be investigated, since nanotube delamination may cause detachment of deposited bone *in vivo*.

## 6 ACKNOWLEDGEMENTS

Funding from the National Sciences and Engineering Research Council (NSERC) Discovery Grant program to KG is gratefully acknowledged. BL was supported by an Ontario Graduate Scholarship, JD and DMB were supported by NSERC. 3D printing was carried out at the Additive Manufacturing Innovation Centre at Mohawk College and anodization at the McMaster Automotive Resource Centre (MARC). Characterizations were performed at the Faculty of Health Science Electron Microscopy Facility, the Canadian Centre for Electron Microscopy, and the Biointerfaces Institute at McMaster University.

## 7 REFERENCES

1. Kasemo B. Biocompatibility of titanium implants: Surface science aspects. *J Prosthet Dent*. 1983;49:832–7.
2. Frazier WE. Metal Additive Manufacturing: A Review. *J Mater Eng Perform*. 2014;23:1917–28.
3. Körner C. Additive manufacturing of metallic components by selective electron beam melting — a review. *Int Mater Rev*. 2016;61:361–77.
4. Pyka G, Burakowski A, Kerckhofs G, Moesen M, Bael S, Schrooten J, et al. Surface Modification of Ti6Al4V Open Porous Structures Produced by Additive Manufacturing. *Adv Eng Mater*. 2012;14:363–70.
5. Gu D, Shen Y. Balling phenomena in direct laser sintering of stainless steel powder: Metallurgical mechanisms and control methods. *Mater Design*. 2009;30:2903–10.
6. Bauer S, Schmuki P, von der Mark K, Park J. Engineering biocompatible implant surfaces Part I: Materials and surfaces. *Prog Mater Sci*. 2013;58:261–326.
7. Davies JE, Mendes VC, Ko J, Ajami E. Topographic scale-range synergy at the functional bone/implant interface. *Biomaterials*. 2014;35:25–35.
8. Warnke PH, Douglas T, Wollny P, Sherry E, Steiner M, Galonska S, et al. Rapid Prototyping: Porous Titanium Alloy Scaffolds Produced by Selective Laser Melting for Bone Tissue Engineering. *Tissue Eng Part C Methods*. 2009;15:115–24.
9. Shaoki A, Xu J, Sun H, Chen X, Ouyang J, Zhuang X, et al. Osseointegration of three-dimensional designed titanium implants manufactured by selective laser melting. *Biofabrication*.

2016;8:045014.

10. Gittens RA, Olivares-Navarrete R, Schwartz Z, Boyan BD. Implant osseointegration and the role of microroughness and nanostructures: Lessons for spine implants. *Acta Biomater.* 2014;10:3363–71.
11. Khosravi N, Maeda A, DaCosta RS, Davies JE. Nanosurfaces modulate the mechanism of peri-implant endosseous healing by regulating neovascular morphogenesis. *Commun Biology.* 2018;1.
12. Puleo D., Nanci A. Understanding and controlling the bone–implant interface. *Biomaterials.* 1999;20:2311–21.
13. Martínez E, Engel E, Planell JA, Samitier J. Effects of artificial micro- and nano-structured surfaces on cell behaviour. *Ann Anat - Anatomischer Anzeiger.* 2009;191:126–35.
14. Ehrenfest DM, Coelho PG, Kang B-S, Sul Y-T, Albrektsson T. Classification of osseointegrated implant surfaces: materials, chemistry and topography. *Trends Biotechnol.* 2010;28:198–206.
15. Shah F, Nilson B, Brånemark R, Thomsen P, Palmquist A. The bone-implant interface – nanoscale analysis of clinically retrieved dental implants. *Nanomed Nanotechnol Biology Medicine.* 2014;10:1729–37.
16. Yavari AS, Wauthle R, Böttger AJ, Schrooten J, Weinans H, Zadpoor AA. Crystal structure and nanotopographical features on the surface of heat-treated and anodized porous titanium biomaterials produced using selective laser melting. *Appl Surf Sci.* 2014;290:287–94.
17. Khudhair D, Bhatti A, Li Y, Hamedani AH, Garmestani H, Hodgson P, et al. Anodization parameters influencing the morphology and electrical properties of TiO<sub>2</sub> nanotubes for living cell interfacing and investigations. *Mater Sci Eng C.* 2016;59:1125–42.
18. Gulati K, Prideaux M, Kogawa M, Lima-Marques L, Atkins GJ, Findlay DM, et al. Anodized 3D–printed titanium implants with dual micro- and nano-scale topography promote interaction with human osteoblasts and osteocyte-like cells. *J Tissue Eng Regen M.* 2017;11:3313–25.
19. Simonelli M, Tse YY, Tuck C. Effect of the build orientation on the mechanical properties and fracture modes of SLM Ti–6Al–4V. *Mater Sci Eng.* 2014;616:1–11.
20. Murphy W, Black J, Hastings G. *Handbook of Biomaterial Properties.* 2016;
21. Niinomi M, Nakai M. Titanium-Based Biomaterials for Preventing Stress Shielding between Implant Devices and Bone. *Int J Biomaterials.* 2011;2011:836587.

22. Huiskes R, Weinans H, Rietbergen B. The Relationship Between Stress Shielding and Bone Resorption Around Total Hip Stems and the Effects of Flexible Materials. *Clin Orthop Relat R.* 1992;274:124–34.
23. Long M, Rack H. Titanium alloys in total joint replacement—a materials science perspective. *Biomaterials.* 1998;19:1621–39.
24. Li Y, Yang C, Zhao H, Qu S, Li X, Li Y. New Developments of Ti-Based Alloys for Biomedical Applications. *Materials.* 2014;7:1709–800.
25. Schwab H, Bönisch M, Giebeler L, Gustmann T, Eckert J, Kühn U. Processing of Ti-5553 with improved mechanical properties via an in-situ heat treatment combining selective laser melting and substrate plate heating. *Mater Design.* 2017;130:83–9.
26. Schwab H, Palm F, Kühn U, Eckert J. Microstructure and mechanical properties of the near-beta titanium alloy Ti-5553 processed by selective laser melting. *Mater Design.* 2016;105:75–80.
27. Zopp C, Blümer S, Schubert F, Kroll L. Processing of a metastable titanium alloy (Ti-5553) by selective laser melting. *Ain Shams Eng J.* 2017;8:475–9.
28. Sabol JC, Pasang T, Misiolek WZ, Williams JC. Localized tensile strain distribution and metallurgy of electron beam welded Ti–5Al–5V–5Mo–3Cr titanium alloys. *J Mater Process Tech.* 2012;212:2380–5.
29. Lee B, Exir H, Weck A, Grandfield K. Characterization and Evaluation of Femtosecond Laser-Induced Sub-micron Periodic Structures Generated on Titanium to Improve Osseointegration of Implants. *Appl Surf Sci.* 2018;441:1034–42.
30. Maher S, Mazinani A, Barati M, Losic D. Engineered titanium implants for localized drug delivery: recent advances and perspectives of Titania nanotubes arrays. *Expert Opin Drug Del.* 2018;15:1021–37.
31. Roy P, Berger S, Schmuki P. TiO<sub>2</sub> Nanotubes: Synthesis and Applications. *Angewandte Chemie Int Ed.* 2011;50:2904–39.
32. Gui Q, Yu D, Li D, Song Y, Zhu X, Cao L, et al. Efficient suppression of nanograss during porous anodic TiO<sub>2</sub> nanotubes growth. *Appl Surf Sci.* 2014;314:505–9.
33. Minagar S, Berndt CC, Wang J, Ivanova E, Wen C. A review of the application of anodization for the fabrication of nanotubes on metal implant surfaces. *Acta Biomater.* 2012;8:2875–88.

34. Park J, Bauer S, von der Mark K, Schmuki P. Nanosize and Vitality: TiO<sub>2</sub> Nanotube Diameter Directs Cell Fate. *Nano Lett.* 2007;7:1686–91.
35. Hamlekhan A, Sinha-Ray S, Takoudis C, Mathew MT, Sukotjo C, Yarin AL, et al. Fabrication of drug eluting implants: study of drug release mechanism from titanium dioxide nanotubes. *J Phys D Appl Phys.* 2015;48:275401.
36. Sallica-Leva E, Jardini AL, Fogagnolo JB. Microstructure and mechanical behavior of porous Ti–6Al–4V parts obtained by selective laser melting. *J Mech Behav Biomed.* 2013;26:98–108.
37. Wang H, Su K, Su L, Liang P, Ji P, Wang C. The effect of 3D-printed Ti6Al4V scaffolds with various macropore structures on osteointegration and osteogenesis: A biomechanical evaluation. *J Mech Behav Biomed.* 2018;88:488–96.
38. Gulati K, Santos A, Findlay D, Losic D. Optimizing Anodization Conditions for the Growth of Titania Nanotubes on Curved Surfaces. *J Phys Chem C.* 2015;119:16033–45.
39. Oh S, Daraio C, Chen L, Pisanic TR, Fiñones RR, Jin S. Significantly accelerated osteoblast cell growth on aligned TiO<sub>2</sub> nanotubes. *J Biomed Mater Res A.* 2006;78A:97–103.
40. Balaur E, Macak JM, Taveira L, Schmuki P. Tailoring the wettability of TiO<sub>2</sub> nanotube layers. *Electrochem Commun.* 2005;7:1066–70.
41. Rupp F, Gittens RA, Scheideler L, Marmur A, Boyan BD, Schwartz Z, et al. A review on the wettability of dental implant surfaces I: Theoretical and experimental aspects. *Acta Biomater.* 2014;10:2894–906.
42. Shin D, Shokuhfar T, Choi C, Lee S-H, Friedrich C. Wettability changes of TiO<sub>2</sub> nanotube surfaces. *Nanotechnology.* 2011;22:315704.
43. Wang R, Hashimoto K, Fujishima A, Chikuni M, Kojima E, Kitamura A, et al. Photogeneration of Highly Amphiphilic TiO<sub>2</sub> Surfaces. *Adv Mater.* 1998;10:135–8.
44. Kokubo T, Takadama H. How useful is SBF in predicting in vivo bone bioactivity? *Biomaterials.* 2006;27:2907–15.
45. Jones NG, Dashwood RJ, Dye D, Jackson M. Thermomechanical processing of Ti–5Al–5Mo–5V–3Cr. *Mater Sci Eng.* 2008;490:369–77.